Preprint Title	Size-Dependent Thermoresponsive Magnetic Core/Shell Nanoparticles for Controlled Doxorubicin Release and Hyperthermia-Assisted Cancer Therapy
Authors	Halima Alem, Dounia Louaguef, Claire Godier, Melanie Emo, Brigitte Vigolo, Khalid Ferji, Damien Mertz, Joelle Bizeau, Klaus M. Seemann, Thomas Gries, Aixa Aguilera Garrido, Zied ferjaoui, Vuanghao Lim and Eric Gaffet
Publication Date	02 Juli 2026
Article Type	Full Research Paper
ORCID® iDs	Halima Alem - https://orcid.org/0000-0002-7918-0504; Brigitte Vigolo - https://orcid.org/0000-0002-1463-0121; Damien Mertz - https://orcid.org/0000-0002-6745-8978; Joelle Bizeau - https://orcid.org/0000-0002-7810-0525; Klaus M. Seemann - https://orcid.org/0000-0002-9103-4809; Thomas Gries - https://orcid.org/0000-0003-4601-2675; Aixa Aguilera Garrido - https://orcid.org/0000-0003-3470-7904; Vuanghao Lim - https://orcid.org/0000-0001-5081-0982; Eric Gaffet - https://orcid.org/0000-0002-6451-3011

Size-Dependent Thermoresponsive Magnetic Core/Shell Nanoparticles for Controlled Doxorubicin Release and Hyperthermia-Assisted Cancer Therapy

Dounia Louaguef [1], Claire Godier [1], Mélanie Emo [1], Brigitte Vigolo [1], Khalid Ferji [2], Damien Mertz[3], Joelle Bizeau[3], Klaus. M Seemann [1], Thomas Gries [1], Aixa Aguilera Garrido[1], Zied Ferjaoui[4], Vuanghao Lim[5], Eric Gaffet [1] and Halima Alem * [1,4]

[1] Institut Jean Lamour (UMR 7198), Université de Lorraine, CNRS, F54011 Nancy, France

[2] Université de Lorraine, CNRS, LCPM, F-54000 Nancy, France.

[3] Institut de physique et de chimie des matériaux, UMR 7504 CNRS – Université de Strasbourg, France

[4] Université Paris Cité, CNRS, INSERM, UTCBS, Unité de Technologies Chimiques et Biologiques pour la Santé, Paris, F-75006 France

[5] Advanced Medical and Dental Institute, Universiti Sains Malaysia, Bertam 13200 Kepala Batas, Penang, Malaysia

* corresponding author: halima.alem@univ-lorraine.fr

Abstract:

Thermoresponsive magnetic core/shell nanoparticles were developed for controlled drug delivery in cancer therapy. Polyhedral $Zn_{0.4}Fe_{2.6}O_4$@$MnFe_2O_4$ nanoparticles with two core sizes (22 and 50 nm) were synthesized and coated with a thermosensitive copolymer shell composed of 2-(2-methoxy)ethyl methacrylate and oligo(ethylene glycol) methacrylate units, $P(MEO_2MA_{60}–OEGMA_{40})$. The copolymer was grafted directly from the nanoparticle surface using aqueous ARGET-ATRP, providing a controlled and environmentally friendly functionalization strategy. Doxorubicin (DOX) was successfully encapsulated within the polymer shell and released upon heating above the lower critical solution temperature (LCST). Structural and compositional characterizations confirmed successful polymer grafting while preserving the crystalline integrity of the magnetic cores. Dynamic light scattering revealed a sharp thermoresponsive transition around 40–42 °C.

Size-dependent magnetic and hyperthermia performances were observed, with larger nanoparticles exhibiting enhanced heating efficiency. Drug release studies in water and physiological medium (DMEM) demonstrated efficient temperature-dependent DOX release with distinct release profiles depending on nanoparticle size, attributed to differences in polymer grafting density and drug loading capacity.

In vitro cytotoxicity assays on human ovarian cancer cells (SKOV-3) showed enhanced antitumoral activity of DOX-loaded nanoparticles compared with free DOX, while unloaded nanoparticles displayed low intrinsic toxicity. These results highlight thermoresponsive magnetic nanoparticles as a promising platform for temperature-responsive drug delivery and hyperthermia-assisted cancer therapy.

Keywords: Polyhedral core/shell MNPs, thermosensitive polymers, hyperthermia, drug delivery, SKOV-3 cells.

1- Introduction:

In the ongoing search for improved cancer therapies, a wide variety of nanoparticles (NPs) have been developed and investigated. Among them, magnetic nanoparticles have attracted particular attention due to their multifunctional capabilities. In addition to the typical advantages of nanocarriers—such as prolonged drug circulation time, enhanced tumor targeting, improved therapeutic efficacy, and reduced side effects—magnetic nanoparticles offer unique features. Their response to external magnetic fields enables targeted guidance toward tumor sites and localized heat generation under alternating magnetic fields, inducing hyperthermia-mediated cancer cell death. Furthermore, they can serve as contrast agents for magnetic resonance imaging (MRI), making them attractive theranostic platforms.[1–8](Abenojar et al., 2016; Jurgons et al., 2006; Mahmoudi et al., 2012; Nguyen, 2011; Sadhukha et al., 2013; Santhosh and Ulrih, 2013; Yigit et al., 2012; Zhang et al., 2018)

Among the different magnetic nanomaterials, FDA-approved superparamagnetic iron oxide nanoparticles (SPIONs)(Li et al., 2013) particularly promising due to their biocompatibility, biodegradability, and relatively low production cost, facilitating potential clinical translation(Abenojar et al., 2016; Ferjaoui et al., 2019; Jamal Al Dine et al., 2017; Kievit and Zhang, 2011). Their magnetic and heating properties strongly depend on parameters such as size, composition, shape, and surface functionalization. Notably, anisotropic or polyhedral nanoparticles have been reported to exhibit enhanced magnetic responses and improved heating efficiency compared to spherical counterparts.(Angelopoulou et al., 2019; Cotin et al., 2019) . SPIONs have also been widely explored as platforms for combined hyperthermia and drug delivery applications [22–24]. In this context, core/shell nanostructures have been developed, where the shell serves multiple functions, including drug loading, colloidal stabilization, improved biocompatibility, and, in some cases, stealth behavior to evade immune recognition.(Ferjaoui et al., 2017a; Shi et al., 2024). The incorporation of thermoresponsive polymers as shell materials is particularly attractive, as they enable controlled drug release in response to temperature variations. These temperature changes can be externally induced, including through magnetic hyperthermia generated by the nanoparticle core.(Ferjaoui et al., 2017b). These polymers are known to exhibit a reversible change in their colloidal behavior depending on temperature. Thus, thermo-responsive polymers-shelled SPIONs enable temperature-controlled drug release upon heating. which is modulated by the application of an external magnetic field.

Thermoresponsive polymers exhibit reversible changes in their physicochemical properties depending on temperature. In systems exhibiting a lower critical solution temperature (LCST), polymer chains are hydrated and soluble below the transition temperature, whereas above the LCST, polymer–polymer interactions dominate, leading to chain collapse and reduced solubility. Conversely, upper critical solution temperature (UCST) systems display the opposite behavior. For biomedical applications, LCST-type polymers are particularly relevant(Pasparakis and Tsitsilianis, 2020),(Doberenz et al., 2020).

In mild hyperthermia-based cancer therapies, the target temperature is typically around 42 °C, which is sufficient to induce cancer cell death while minimizing damage to surrounding healthy tissues. Therefore, thermoresponsive polymers with LCST values close to this temperature range are highly desirable. Copolymers based on 2-(2-methoxyethyl methacrylate) (MEO_2MA) and oligo(ethylene glycol) methacrylate (OEGMA) are especially promising due to their biocompatibility and tunable LCST. Increasing the OEGMA content raises the LCST, whereas increasing the MEO_2MA fraction lowers it, allowing precise control of the transition temperature (Ferjaoui et al., 2017a),(Jamal Al Dine et al., 2017),(Santos et al., 2021).

In this study, we report the development of thermoresponsive magnetic nanocarriers for the controlled delivery of doxorubicin (DOX), an anticancer drug. Polyhedral $Zn_{0.4}Fe_{2.6}O_4$@$MnFe_2O_4$ core/shell nanoparticles with two distinct sizes were synthesized and functionalized with a P(MEO_2MA_{60}–$OEGMA_{40}$) copolymer shell via ARGET-ATRP. The

LCST-driven phase transition of the polymer enables temperature-triggered drug release at approximately 42 °C. In addition, the magnetic cores allow heat generation under an alternating magnetic field, providing a potential strategy for combined hyperthermia and chemotherapy.
We investigate the structural, magnetic, and thermoresponsive properties of the system, as well as DOX release profiles and cytotoxic effects on SKOV-3 ovarian cancer cells. This multifunctional nanoplatform demonstrates potential for localized, temperature-controlled drug delivery with reduced systemic toxicity.

2- Materials and methods:

Materials:

Tetramethylammonium hydroxide pentahydrate (TMAH, 99.8%), (3-aminopropyl) triethoxysilane (APTES), Triethylamine (TEA ≥99.5%), α-bromoisobutyryl bromide (BIBB), toluene (laboratory reagent, >99.3%), 2-(2-methoxy) ethyl methacrylate (MEO_2MA) (98%), oligo (ethylene glycol) methacrylate (OEGMA) (98%), and dimethyl sulfoxide (DMSO) (>99.8%) were purchased from Sigma-Aldrich and chloromethyl phenylethyl triméthoxysilane (CMPETMS, > 95% from Gelest. Doxorubicin (DOX) was provided in the form of DOXIL (2 mg/mL) byAccord laboratory.

a- Synthesis of $Zn_{0.4}Fe_{2.6}O_4$ @ $MnFe_2O_4$ NPs:

$Zn_{0.4}Fe_{2.6}O_4$@$MnFe_2O_4$ nanoparticles were synthesized following a previously reported method (Louaguef et al., 2025). Briefly, $Zn_{0.4}Fe_{2.6}O_4$ cores were prepared via thermal decomposition of iron(III) and zinc(II) acetylacetonates in benzyl ether in the presence of oleic acid under an argon atmosphere. The reaction mixture was heated to 290 °C at a rate of 5 $°C \cdot min^{-1}$ and maintained for 30 min.
After cooling to room temperature, nanoparticles were precipitated with ethanol, collected by centrifugation, washed twice, and redispersed in toluene.
The $MnFe_2O_4$ shell (~5 nm) was grown via a seeded growth approach using iron(III) and manganese(II) acetylacetonates under similar conditions. Two nanoparticle sizes (22 and 50 nm) were obtained.

b- Coating of $Zn_{0.4}Fe_{2.6}O_4$ @ $MnFe_2O_4$ (22nm) with CMPETMS (NPs@ CMPETMS):

$Zn_{0.4}Fe_{2.6}O_4$@$MnFe_2O_4$ nanoparticles (100 mg) were dispersed in 30 mL of toluene and sonicated for 15 min. CMPETMS (0.4 mmol) was added, and the mixture was heated at 50 °C under argon with magnetic stirring. 2 mL of TMAH solution was used. This solution was prepared by dissolving 217.5 mg of tetramethylammonium hydroxide pentahydrate (TMAH) in 6 mL of ethanol and the reaction was maintained for 24 h.

After cooling, nanoparticles were recovered by centrifugation, washed twice with toluene, and redispersed. A second silanization step was performed under similar conditions to ensure sufficient surface functionalization (Figure1-(a)).

c- Coating of $Zn_{0.4}Fe_{2.6}O_4$@ $MnFe_2O_4$ (50nm) with APTES-BIBB (NPs@ APTES-BIBB) :

Nanoparticles (100 mg) were dispersed in toluene and sonicated for 15 min. Subsequently, 90 µL of (3-aminopropyl)triethoxysilane (APTES) was added dropwise, and the mixture was stirred at 50 °C for 24 h under an argon atmosphere. The particles were then collected by centrifugation, washed several times with toluene, and redispersed in anhydrous toluene. Next, 150 µL of triethylamine (TEA) was added, and the reaction mixture was cooled to 0 °C. Afterward, 75 µL of α-bromoisobutyryl bromide (BIBB) was added dropwise. The reaction was maintained under stirring for 30 min at 0 °C and then allowed to proceed for 24 h at room temperature. Finally, the functionalized nanoparticles were recovered by centrifugation and thoroughly washed with ethanol and acetone to remove any unreacted reagent

(Figure1-(b)).

d- P(MEO_2MA_{60}-$OEGMA_{40}$) NPs Coating via Copolymer Surface Polymerization

Functionalized nanoparticles (50 mg) were dispersed in 30 mL of dimethyl sulfoxide (DMSO) by sonication. Subsequently, 1.16 mL of 2-(2-methoxyethyl) methacrylate (MEO_2MA) and 1.14 mL of oligo(ethylene glycol) methacrylate (OEGMA) were added dropwise to the nanoparticle suspension under continuous stirring. Then, 200 µL of the $CuBr_2$/TPMA catalyst solution in DMSO (0.884 mmol $CuBr_2$ and 4.3 mmol TPMA) was added. The reaction mixture was purged with argon for 30 min to remove dissolved oxygen. Polymerization was initiated by the addition of hydrazine and allowed to proceed under an argon atmosphere for 2 h at room temperature. Upon completion, the reaction mixture was poured into deionized water and heated to 50 °C to induce precipitation of the polymer-grafted nanoparticles. Finally, the nanoparticles were collected by centrifugation and washed twice with hot deionized water to remove residual monomers and unreacted species (Figure 1).

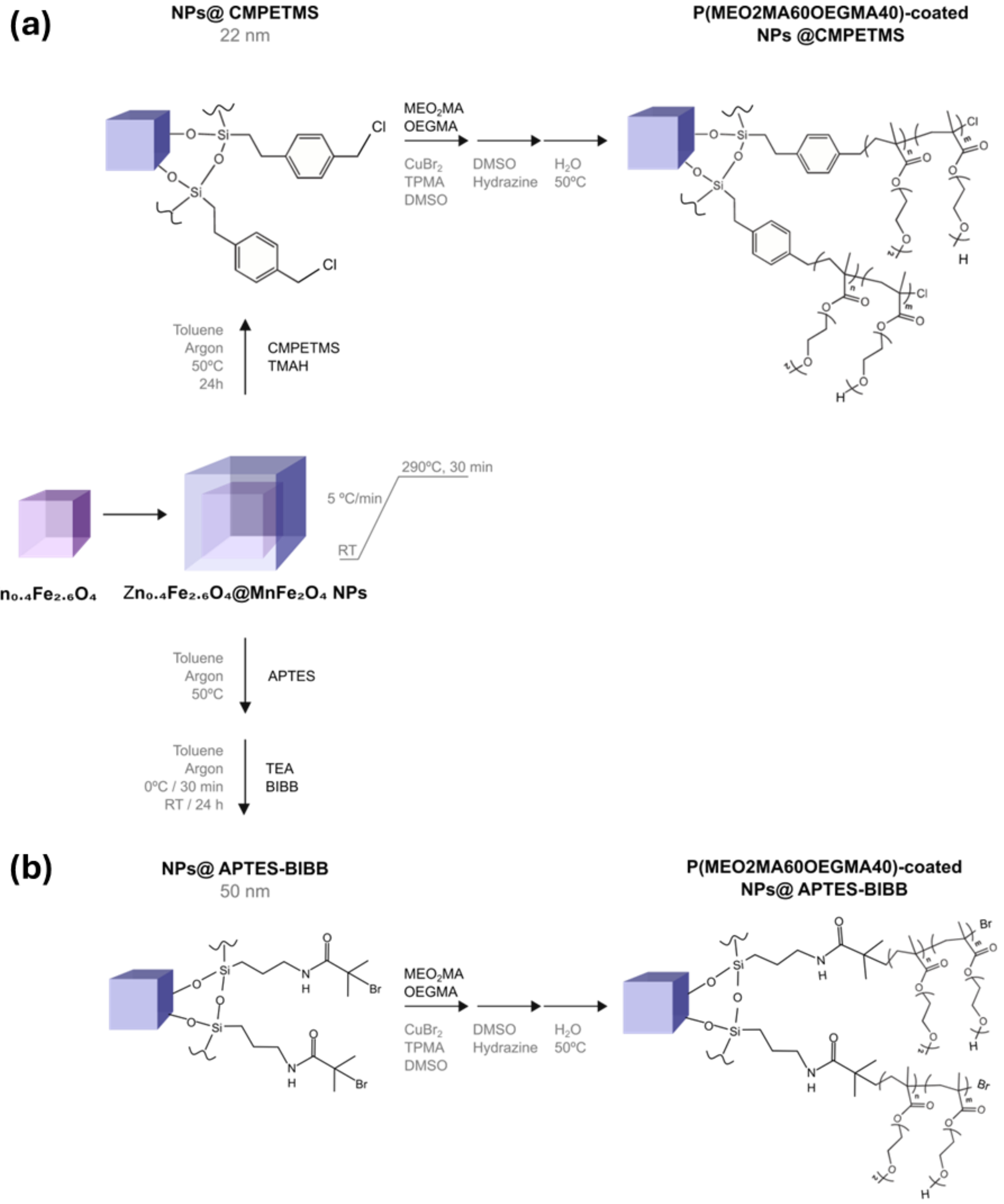

Figure 1: Functionalized NPs @CMPETMS (a) and NPs@ APTES-BIBB (b) by P($MEO_2MA_{60}OEGMA_{40}$)

e- Encapsulation of Doxorubicin in NPs@P($MEO_2MA_{60}OEGMA_{40}$):

To load Doxorubicin (DOX) in the NPs, 2.5 mg of NPs@P($MEO_2MA_{60}OEGMA_{40}$) were dispersed in in 5 ml of MilliQ water and 5 mL of physiological medium (DMEM) by sonication. Then, 5 ml of DOX0.5 mg.mL-1 were added and the mixture was stirred in the dark at 4°C for 24 h. After 24 h, the DOX-loaded NPs were collected by centrifugation and washed with Milli-Q water. The presence of Dox in the supernatant was checked by absorbance at 480 nm and NPs were washed for at least 4 times, until no DOX signal was detected by UV-visible spectroscopy. Finally, the Dox-loaded NPs @ P($MEO_2MA_{60}OEGMA_{40}$) were dispersed in 3 mL of water and the Dox concentration was measured by UV-visible spectroscopy as previously described. The concentrqtion of DOX was determined by comparing of the absorbance data obtained to a calibration curve. Then, drug loading rate (DLC) and the encapsulation efficiency (DLE) were calculated using Equations (1) and (2), respectively.

f- Doxorubicin release kinetics:

DOX release was evaluated as a function of temperature and time by measuring the absorbance at 480 nm. For temperature-dependent studies, samples were heated between 35 and 50 °C. For kinetic studies, release was monitored at 37 °C and 42 °C for up to 50 h. The data were fitted using zero-order, first-order, and Higuchi models.

$$DLC\ \% = \frac{\text{mass of DOX encapsulated in NPs}}{\text{NPs mass}} \times 100 \qquad (1)$$

$$DLE\ \% = \frac{\text{mass of DOX encapsulated in NPs}}{\text{total mass of DOX}} \times 100 \qquad (2)$$

The release results obtained were compared to three empirical mathematical models that describe the nature of the drug release mechanism of NPs @ P($MEO_2MA_{60}OEGMA_{40}$):

Zero order model (Eq. 3): This represents a release rate independent from the concentration of the dissolved drug, and is represented by the following equation:

$$M_t = M_0 + K_0 .\ t \qquad (3)$$

Where M_t is the quantity of drug released at time t, M_0 is the initial quantity of the active ingredient (generally $M_0 = 0$), and K_0 is the zero-order release constant.

First order model (Eq. 4): This model represents a release rate depending on the concentration of dissolved drug.

$$L(M_0 - M_t) = Ln(M_0) - K_1.\, t \qquad (4)$$

Where M_0 is the quantity of drug before dissolution, M_t is the quantity of drug released at time t, and K_1 is the first-order release constant.

Higuchi model (Eq. 5): This model defines release by diffusion and describes release from solid matrices.

$$M_t = K_h.\, \sqrt{t} \qquad (5)$$

Where M_t is the quantity of the drug released at time t and K_h is the speed constant. The release was carried out by diffusion and did not depend on M_0.

g- Characterization of NPs@P($MEO_2MA_{60}OEGMA_{40}$):

Fourier transform infrared spectroscopy (FTIR): The FTIR spectra were recorded using a commercial Agilent FTIR 680 spectrometer in the attenuated total reflection (ATR) mode. The spectra were acquired from 400 to 4000 cm^{-1} with a spectral resolution of 4 cm^{-1}. The reference spectra were acquired before each acquisition to determine the absorption spectra under ambient conditions. Each measurement was averaged over 200 scans in the continuous mode to improve the signal-to-noise ratio.

Thermogravimetric Analysis (TGA): TGA analyses were carried out using a Setaram Setsys Evolution 1750. The experiments were performed using dry air as the carrier gas (flow rate 20 $mL.min^{-1}$) and a temperature ramp of 5°C. min^{-1} from room temperature to 550°C.

High-resolution transmission electron microscopy (HR-TEM): Transmission electron microscopy (TEM) images were obtained using a JEOL JEM-ARM 200F Cold FEG microscope operating at 200 kV and equipped with a spherical aberration (Cs) probe corrector. For each sample, an average of 30-40 images were taken on different areas randomly selected.

Dynamic Light Scattering (DLS): Light scattering measurements were performed using an ALV/ CGS-3 compact goniometer system, equipped with an ALV-7004 digital multiple τ correlator and an optimized He-Ne laser with an output power of 22 mW operating at a length À = 632.8 nm. During analysis, the sample was kept in a toluene bath to maintain a constant sample temperature (from 20 to 50°C) and to suppress reflections from the glass-air-interface of the sample cell. Scattered light was detected at scattering angles of $30° \leq \theta \leq 150°$, corresponding to the scattering vector regime of 0.00459 $nm^{-1} \leq q \leq 0.00255$ nm^{-1}. which can be calculated using Equations (6 and 7), where n is the refractive index of the solvent (water).

$$q = \frac{4Mn}{\lambda} sin \frac{\theta}{2} \quad \text{(Eq. 6)}$$

In DLS, autocorrelation functions were analyzed in terms of the relaxation time distribution (τ) as a function of the REPES routine. The mean hydrodynamic radius (R_H) was estimated using the Stokes-Einstein equation (7), where D_0 is the nanoobjects determined from the slope of the q2 dependence of the relaxation rate (<Γ> =Dq2), kB is the Boltzmann constant, T is the absolute temperature, and ηs is the viscosity of the solvent (water).

$$RH = \frac{KB\ T}{6M\ \eta s\ D0} \quad \text{(Eq. 7)}$$

Superconducting Quantum Interference Device (SQUID): The magnetism measurements described in this chapter and the ZFC/FC curves for the NPs were obtained using an MPMS3 Squid magnetometer (Quantum Design). The vibration amplitude used was5 nm and the integration time was 2 sec. The samples were analyzed in gelatin capsules fixed in a glass straw.

Magnetic hyperthermia: Specific absorption rate (SAR) measurements were performed using a calorimetric method on a DM 100 instrument and DM applicator (Nanoscale Biomagnetics™, nB, Zaragoza, Spain) using the MaNIaC software (Nanoscale Biomagnetics™). 1 mL of a solution containing the NPs dispersed in toluene (5 $mg.mL^{-1}$) was placed in vials suitable for this measurement and an alternating magnetic field of 536.5 kHz / 300 Gauss or 796 kHz / 200 Gauss was applied. The temperature increase was recorded for 160 s. The SAR value was then calculated using the method described by *Perigo et al* (Périgo et al., 2013), the ΔT=f(t) curve was fitted with a second-order polynomial function of the form $y=a+b1*x+b2*x^2$, where b1 corresponds to [dT/dt]t=0. SAR was calculated using equation 8:

$$SAR\ (W/g) = \frac{m_{toluene} * Cp_{toluene}}{m_{particles}} * [\frac{dT}{dt}]_{t=0} \quad \text{(Eq. 8)}$$

where $m_{toluene}$ and $Cp_{toluene}$ are the mass (g) and thermal capacity ($J.g^{-1}.\ K^{-1}$) of the sample, m particles is the mass of magnetic nanoparticles present in the sample (g), and [dT/dt] t=0 is the function derived from the temperature at t = 0 ($K.s^{-1}$).

In vitro cytotoxicity: SKOV-3 cells (ovarian adenocarcinoma-derived cell line) were purchased from Sigma-Aldrich and cultured in DMEM supplemented with 10% (v/v) fetal bovine serum (SVF), 2% L-glutamine, 1% penicillin-streptomycin, and 0.05% amphotericin B. All cell culture reagents were supplied by Sigma-Aldrich (St Louis, MO, USA). The cell line was routinely cultured in T75 flasks at 37°C and 5% CO_2 and passaged twice a week. To assess the cytotoxicity of 22 and 50 nm NPs @ $P(MEO_2MA_{60}OEGMA_{40})$, SKOV-3 cells were seeded in 96-well plates ($2*10^4$ cells per well). After 24 h, cells were incubated with 22 and 50 nm NPs @ P($MEO_2MA_{60}OEGMA_{40}$) at different concentrations (ranging from 3.125 to 100 µg.mL^{-1}), free DOX (ranging 0.5 to 5.29 µg.mL^{-1}) and NPs @ DOX(Dox concentration ranging from to) for 5, 24, and 72 h at 37°C or 42°C . After the incubation time with the corresponding sample, the cellular viability was analyzed by using WST-1assay. Briefly, 10 µL of WST-1 were added per well, and cells were incubated at 37°C for 1 h. Finally, the absorbance was recorded using a spectrophotometer at 480 nm. Non-treated cells were used as 100% viability control.

3- Results and discussion:

a- Caracterization of NPs @ P($MEO_2MA_{60}OEGMA_{40}$):

- Fourier transform infrared spectroscopy (FTIR):

The grafting of CMPETMS and the copolymer P($MEO_2MA_{60}OEGMA_{40}$) onto the surface of 22 nm Zn0.4Fe2.6O4@ MnFe2O4 NPs and the grafting of APTES with P($MEO_2MA_{60}OEGMA_{40}$) on the surface of 50 nm Zn0.4Fe2.6O4@ MnFe2O4 NPs was confirmed by Fourier transform infrared spectroscopy. The results as a function of the NP diameter are presented in **Figure 2.**

The NP-CMPETMS spectrum (Figure 2, black) shows a characteristic peak for the Fe–O bond(Saha et al., 2025) at 560 cm^{-1} and a second band at 946 cm^{-1}, which is attributed to the vibrations of the Fe-Si-O bonds, proving that the surface of the NPs is indeed modified by silane(Wang and Shaw, 2014). The presence of silane was also confirmed by the elongation vibrations of the aromatic C-C bonds at 1485 cm^{-1} and C-H stretching vibrations at 3024 cm^{-1}. In the red spectrum of $Zn_{0.4}Fe_{2.6}O_4$@ $MnFe_2O_4$ @CMPETMS@P($MEO_2MA_{60}OEGMA_{40}$), the presence of the copolymer was confirmed by the absorption band located between 2900 and 2980 cm^{-1} which is attributed to the C-H vibrational bond. Another intense band, which characterizes the C=O vibrational bonds, is located at 1700 cm^{-1}, and the C-C and C-O vibrational bonds are present at 1400 and 1100 cm$^{-1.}$

The blue spectrum shows an average band of N-H bonds and an intense band of C-H bonds, indicating that APTES was bound to the surface of the NPs. The presence of APTES was strongly confirmed by the CO-Br, NH-CO, C-N, Si-O, and C-Br bonds at 1683, 1645, 1244, 1013, and 767 cm^{-1}, respectively. The green spectrum of NPs-APTES@ P($MEO_2MA_{60}OEGMA_{40}$) confirms the successful functionalization of NPs-APTES with the P($MEO_2MA_{60}OEGMA_{40}$) copolymer via the C=O and C-O vibrational bonds located at 1730 and 1225 cm^{-1} respectively.

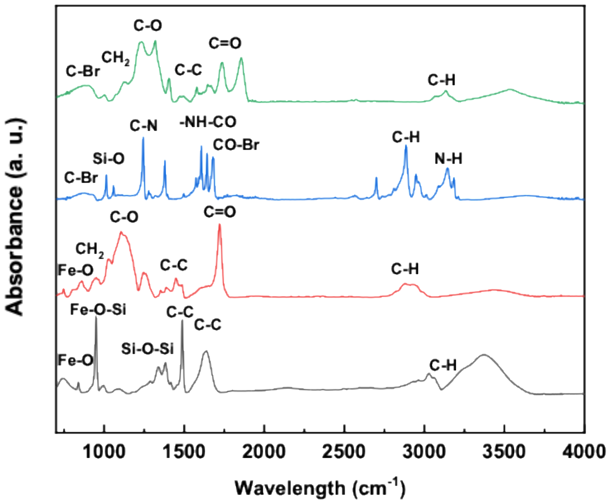

Figure 2: FTIR spectra of NPs-CMPETMS (black), NPs-CMPETMS@ P(MEO$_2$MA$_{60}$OEGMA$_{40}$) (red), NP-APTES (blue), NPs-APTES@ P(MEO$_2$MA$_{60}$OEGMA$_{40}$) (green).

- **Thermogravimetric analysis (TGA):**

The amount of copolymer grafted onto the particle surface is expected to impact on the amount of drug that can be encapsulated. Given that inorganic Zn0.4Fe2.6O4@ MnFe2O4 cores are expected to be stable when heated until 550 °C, TGA analysis was used to determine the amount of copolymer grafted to the surface of both 22 nm and 50 nm NPs @ P(MEO$_2$MA$_{60}$OEGMA$_{40}$). The thermograms of 22 nm and 50 nm NPs @ P(MEO$_2$MA$_{60}$OEGMA$_{40}$) are shown in **Figure 3.**

The general thermogram profile of 22 nm and 50 nm NPs@ P(MEO$_2$MA$_{60}$OEGMA$_{40}$) are quite similar. They show two main weights loss domains illustrated in the figure by zone (I) and zone (II). In zone (I), the weight loss in the low temperature domain (below 100-110 °C) probably originates from dehydration since the NPs @ P(MEO$_2$MA$_{60}$OEGMA$_{40}$) were not stored dried conditions and thus exposed to natural humidity and the P(MEO$_2$MA$_{60}$OEGMA$_{40}$) is highly hydroscopic. The related loss of water is of comparable amount for the two produced samples, *i.e.* 28 and 22 % for 22 nm and 50 nm NPs@ P(MEO$_2$MA$_{60}$OEGMA$_{40}$), respectively. In the domain (II), from 200°C to 550°C, the weight loss is attributed to the decomposition of the P(MEO$_2$MA$_{60}$OEGMA$_{40}$) copolymer part of the samples which is of 47 and 65 % for NPs @ P(MEO$_2$MA$_{60}$OEGMA$_{40}$) 22 and 50 nm, respectively. In agreement with the preparation procedure where both 22 nm and 50 nm NPs were exposed to the same copolymer concentration the greater surface area of the 50 nm NPs results in a higher amount of grafted P(MEO$_2$MA$_{60}$OEGMA$_{40}$) chains compared to the 22 nm NPs.

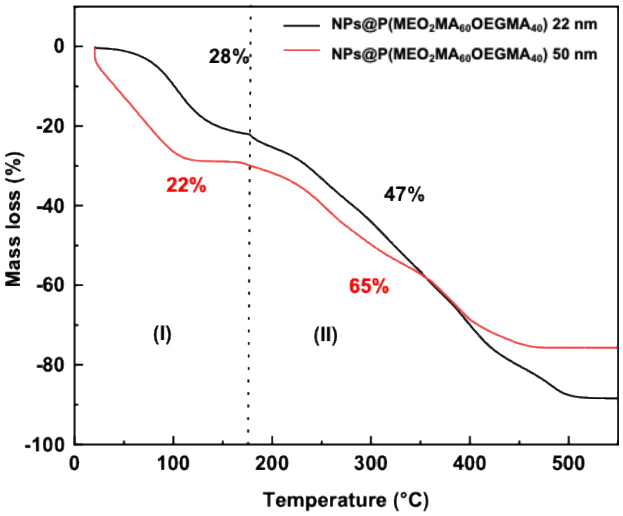

Figure 3: TGA curves of 22 (red) and 50nm (black) NPs@ P(MEO$_2$MA$_{60}$OEGMA$_{40}$)

- **Transmission Electron Microscopy (TEM) :**

High-resolution transmission electron microscopy (HR-TEM) was used to characterize both 22 and 50nm Zn$_{0.4}$ Fe$_{2.6}$ O$_4$@ MnFe$_2$O$_4$ NPs and study their crystalline stability after modification of their surfaces with silane and the copolymer P(MEO$_2$MA$_{60}$OEGMA$_{40}$). **Figure 4** presents the HR-TEM images of Zn$_{0.4}$Fe$_{2.6}$O$_4$@ MnFe$_2$O$_4$ NPs before and after functionalization by the P(MEO$_2$MA$_{60}$OEGMA$_{40}$) copolymer (1) with their electron diffraction patterns (2) and their size distribution histograms (3).

The histograms are based on data from 50 to 100 NPs from each sample, taken randomly on the HR-TEM grid. The distributions were fitted using a Gaussian distribution. Images (1a) and (1c) show the Zn$_{0.4}$Fe$_{2.6}$O$_4$@ MnFe$_2$O$_4$ NPs of 22 and 50 nm respectively before modification with the P(MEO$_2$MA$_{60}$OEGMA$_{40}$) copolymer. The Zn$_{0.4}$Fe$_{2.6}$O$_4$@ MnFe$_2$O$_4$ NPs functionalized with the P(MEO$_2$MA$_{60}$OEGMA$_{40}$) copolymers retained their particle sizes of 22 nm (1b) and 50 nm (1d), as well as their original morphologies. The smaller particles (22 nm) exhibit a polyhedral-like shape, whereas the larger ones (50 nm) present a flower-like or clustered morphology. The electron diffraction patterns of Zn$_{0.4}$Fe$_{2.6}$O$_4$@MnFe$_2$O$_4$ and NPs @P(MEO$_2$MA$_{60}$OEGMA$_{40}$) of 22 and 50 nm are displayed on images (2a), (2b), (2c) and (2d) of Figure 4. These patterns exhibit spots characteristic of a crystalline material. The corresponding d-spacing can be attributed to the polyhedral magnetite. No noticeable difference can be seen before and after modification with copolymer, suggesting that the functionalization of the NPs did not affect their crystalline structure.

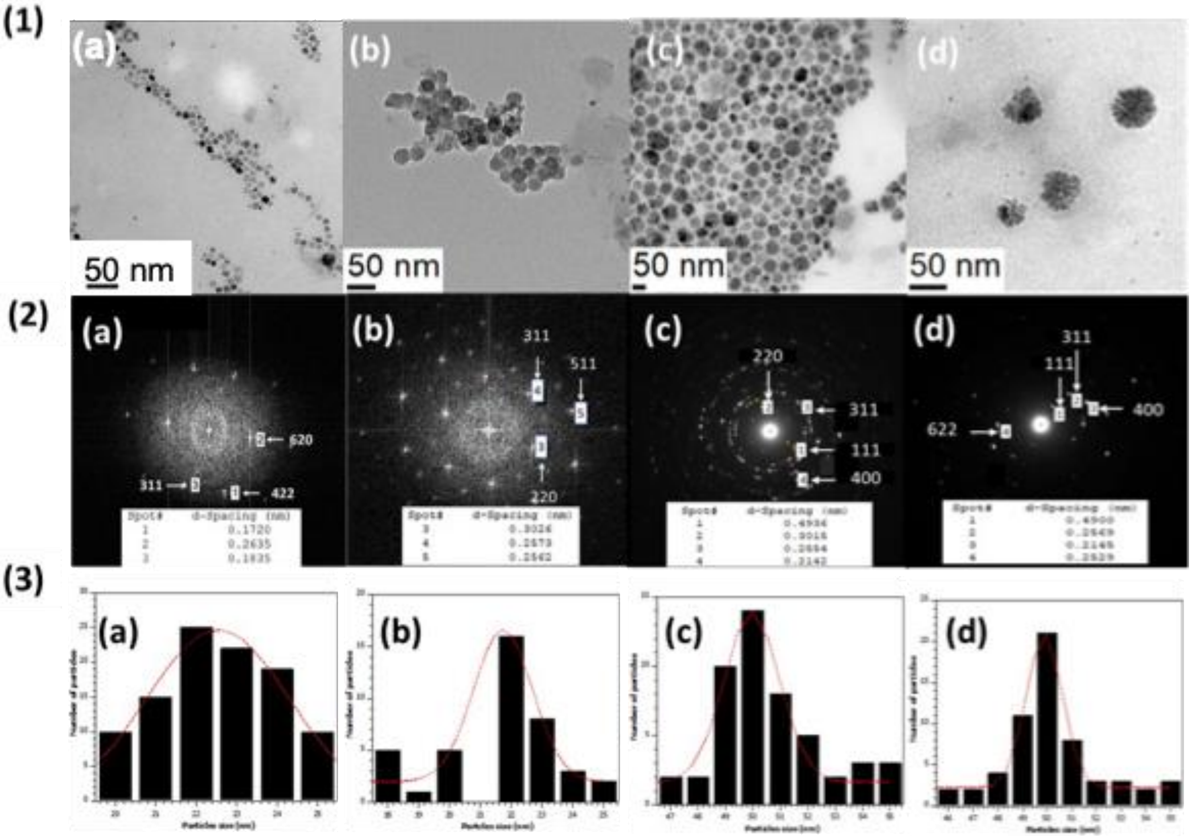

Figure 4: TEM micrographs (1), electron diffraction pattern (2) and size distribution histograms (3) of $Zn_{0.4}$ $Fe_{2.6}$ O_4@ $MnFe_2O_4$ NPs 22 nm (1a), (2a) and (3a). NPs@ P($MEO_2MA_{60}OEGMA_{40}$) 22 nm (1b), (2b) and (3b). NPs $Zn_{0.4}$ $Fe_{2.6}$ O_4@ $MnFe_2O_4$ 50 nm (1c), (2c) and (3c). NPs @P($MEO_2MA_{60}OEGMA_{40}$) 50 nm (1d), (2d) and (3d).

- **Dynamic light scattering (DLS) :**

Dynamic light scattering (DLS) was used to monitor the temperature-dependent evolution of the hydrodynamic radius (R_H) of NPs@ P(MEO_2MA_{60}-$OEGMA_{40}$) with core sizes of 22 nm (a) and 50 nm (b) dispersed in water. Measurements were performed across a temperature range of 20 °C to 50°C (**Figure 5).** Below 40°C, the R_H remained relatively stable for both nanoparticle sizes. However, above this threshold, a marked decrease in R_H was observed until a plateau was reached, indicating a structural transition of the polymer shell. This behavior corresponds to the LCST of the P(MEO_2MA_{60}-$OEGMA_{40}$) copolymer in aqueous media. Below the LCST (40°C), the grafted polymer chains are hydrophilic and highly solvated due to hydrogen bonding with water, leading to an expanded, swollen corona. Above the LCST, these interactions are disrupted, causing the polymer chains to collapse into a more compact, hydrophobic conformation and reducing the overall hydrodynamic size of the nanoparticles.

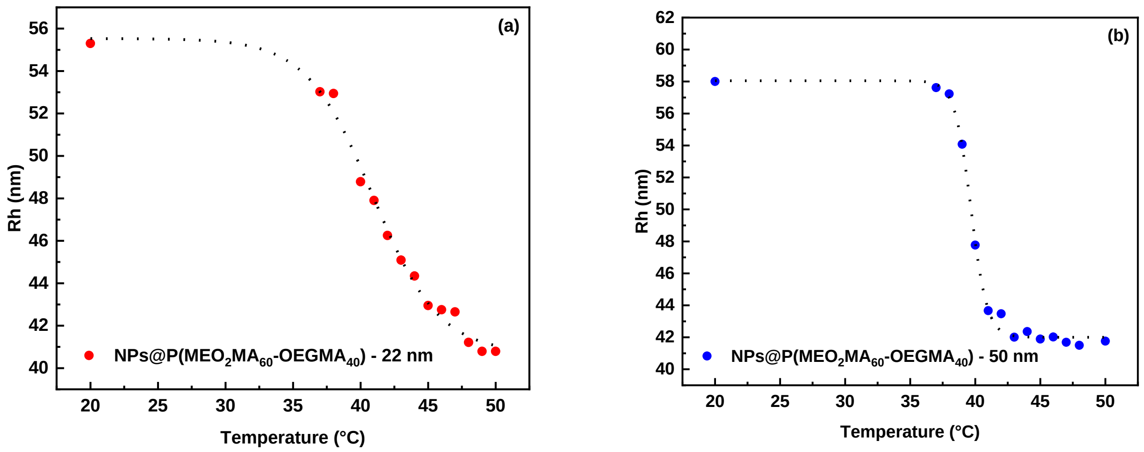

Figure 5: Colloidal behavior of NPs @ P($MEO_2MA_{60}OEGMA_{40}$) 22nm (a) and 50nm (b) as a function of temperature.

- **Magnetic properties of NPs@ P($MEO_2MA_{60}OEGMA_{40}$) :**

Magnetic saturations of both 22 and 50 nm $Zn_{0.4}Fe_{2.6}O_4$@$MnFe_2O_4$ NPs before and after functionalization as a function of the magnetic field were performed using SQUID. Magnetic measurements were performed as a function of the magnetic field (7 Tesla) at a constant temperature of 310 K. The measurement results are presented in **Figure 6**.

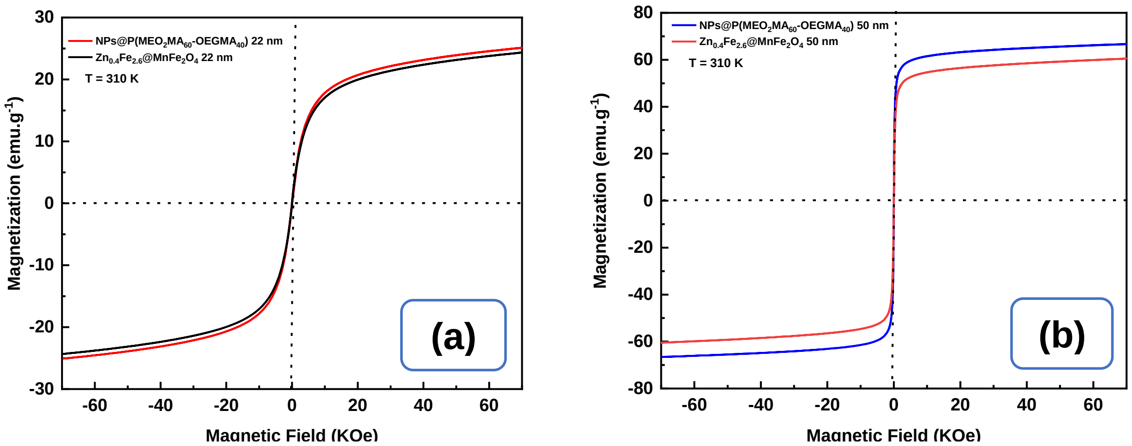

Figure 6: Magnetization values as a function of magnetic field of $Zn_{0.4}Fe_{2.6}O_4$@$MnFe_2O_4$ NPs and NPs@P($MEO_2MA_{60}OEGMA_{40}$) of 22 nm (a) and 50 nm (b).

The obtained results show that the 22 **(Figure 6(a))** and 50nm **(Figure 6(a))** Zn0.4$Fe_{2.6}O_4$@ $MnFe_2O_4$ NPs and NPs @ P($MEO_2MA_{60}OEGMA_{40}$) possess superparamagnetic properties.

The superparamagnetic effect of NPs@ P($MEO_2MA_{60}OEGMA_{40}$) is driven by the magnetic core of the NPs and not by the polymeric layer(Dine, n.d.). The magnetic saturation values of $Zn_{0.4}Fe_{2.6}O_4$@ $MnFe_2O_4$ NPs and NPs@ P($MEO_2MA_{60}OEGMA_{40}$) 22 nm were 25 and 23 emu.g^{-1} respectively and 51 and 48emu/g for $Zn_{0.4}Fe_{2.6}O_4$@ $MnFe_2O_4$ NPs and NPs@ P($MEO_2MA_{60}OEGMA_{40}$) 50 nm respectively.

The slight decrease in Ms values after functionalization from 25 to 23 emu.g^{-1} and from 51 to 48 emu.g^{-1} for both 22 and 50 sized NPs respectively can be attributed to the increase in the non-magnetic polymer fraction, which contributes to the total sample mass used for normalization. This interpretation is supported by TGA analysis (Figure 4), indicating polymer mass fractions of approximately 47% and 65% for the 22 and 50 nm NPs, respectively. It is important to note that the magnetization values reported here are normalized to the total mass of the NPs (core + polymer shell) and therefore do not necessarily reflect changes in the intrinsic magnetic properties of the inorganic core.

Figure 7 shows the ZFC /FC (zero field cooling/field cooling) curves at a constant magnetic field of 25Oe for both 22 (a) and 50 nm (b) NPs @ P(MEO2MA60OEGMA40).

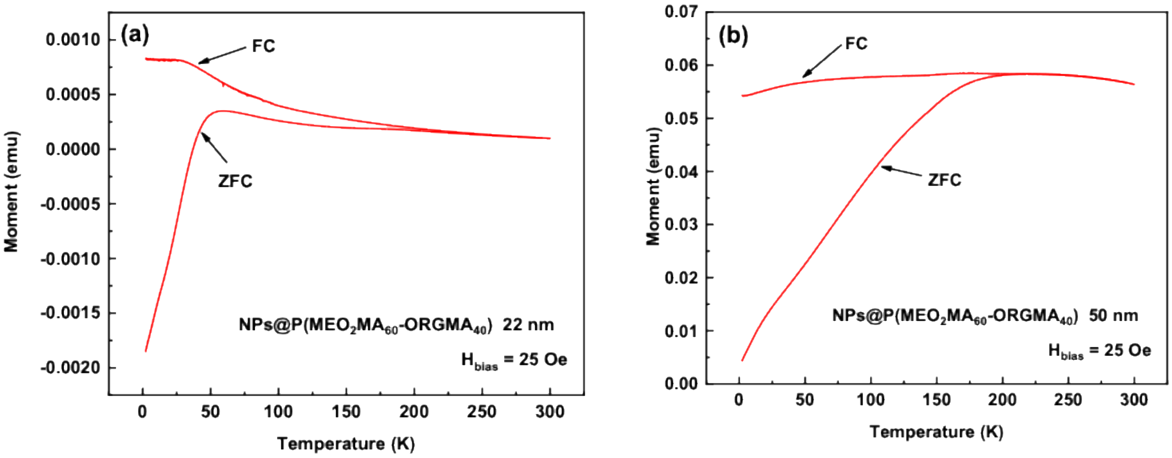

Figure 7: ZFC/FC curves of both 22 nm (a) and 50nm (b) NPs @ P($MEO_2MA_{60}OEGMA_{40}$)

Both nanoparticle systems exhibit a maximum in the ZFC curves, corresponding to the blocking temperature, which separates the blocked magnetic regime (T ≤ TZFCmax) from the superparamagnetic regime (T ≥ TZFCmax). The blocking temperatures were estimated to be 220 ± 10 K and 225 ± 10 K for the 22 nm **(7-(a))** and 50 nm NPs **(7-(b))**, respectively. The slight differences observed in the ZFC/FC profiles may be related to variations in particle size distribution and interparticle interactions. However, no definitive conclusion can be drawn from these measurements alone. Further investigations, such as AC susceptibility measurements, would be required to confirm the presence of interparticle magnetic interactions.

b- Doxorubicine loaded nanoparticles studies:

Fourier transform infrared (FTIR) analysis of NPs @ P($MEO_2MA_{60}OEGMA_{40}$) loaded with DOX:

FTIR analysis was performed to study the interaction of DOX with the copolymer. **Figure 8** shows the FTIR spectra of NPs@ P(MEO_2MA_{60}-$OEGMA_{40}$) (blue line), DOX (Ferjaoui, n.d.) (red line), and NPs @ DOX (black line). The DOX spectrum shows an intense broad band at 3419 cm^{-1} which corresponds to stretching vibrations of O-H in hydroxyl groups. A C-H bond was present at 2933 cm^{-1}. At 1727 cm^{-1} and 1622 cm^{-1} the spectrum shows two bands attributed to the stretching vibrations of C=O and bending vibrations of N-H in NH_2 respectively. The bands recorded at 1417, 1255, 1109 and 990 cm^{-1} correspond to C=C, C-N, C-O, and C=C bonds, respectively, in DOX’s aromatic fractions. The spectrum of NPs @ DOX (black line) shows peaks at 3400, 2898, 1421 and 1100 cm^{-1} characteristic of the O-H, C-H, C=C, and C-O bonds, which represent the copolymer chains grafted onto the surface of the NPs.

The presence of DOX in NPs @ P($MEO_2MA_{60}OEGMA_{40}$) was confirmed by the C=O, N-H, and C-N bonds recorded at 1720, 1645 and 1234 cm^{-1}, respectively.

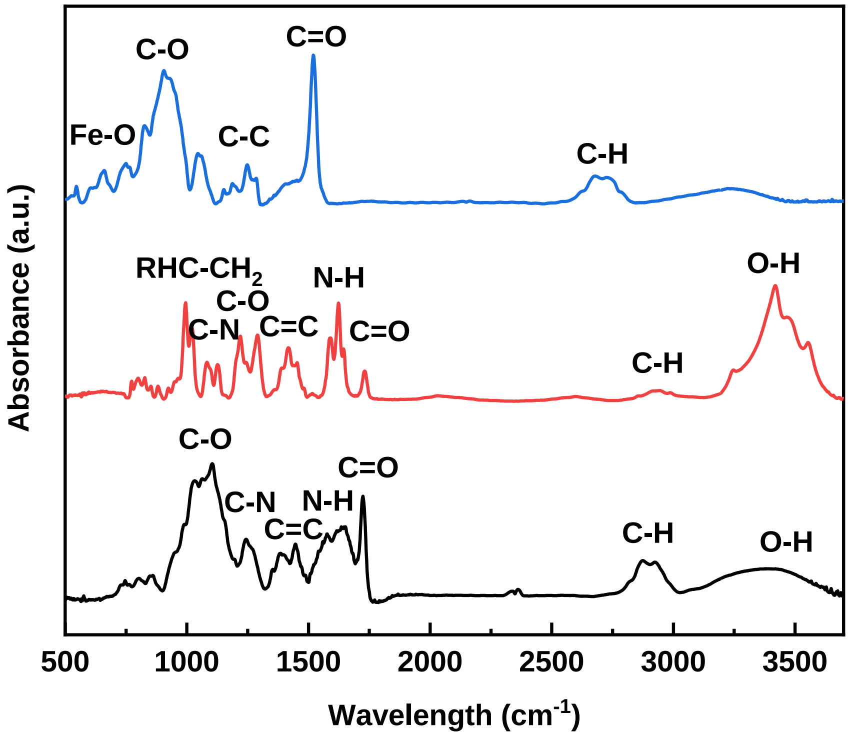

Figure 8: FTIR spectra of NPs@ P(MEO$_2$MA$_{60}$OEGMA$_{40}$) (blue), DOX (red) and NPs@ P(MEO$_2$MA$_{60}$OEGMA$_{40}$) loaded with DOX (black).

DOX release profile:

DOX release as function of temperature:

The release of DOX from NPs @ P(MEO$_2$MA$_{60}$OEGMA$_{40}$) was studied as a function of temperature. The results of this study are represented in **(Figure 9)**.

The release of DOX from NPs @ P(MEO$_2$MA$_{60}$OEGMA$_{40}$) is linked to the lower critical solution temperature (LCST) of the polymeric shell. Around this transition temperature, the copolymer undergoes a coil-to-globule transition driven by a balance between polymer–solvent and polymer–polymer interactions(Saeki et al., 1976).Below the LCST, polymer–solvent interactions dominate, resulting in a hydrated and expanded polymer structure. In contrast, above the LCST, polymer–polymer interactions become predominant, leading to chain collapse, reduced solubility, and the expulsion of water from the polymer network. This structural transition facilitates the diffusion and release of DOX from the polymer shell(Pasparakis and Tsitsilianis, 2020).

To evaluate this behavior, the temperature was increased from 37 to 50 °C, with each temperature maintained for 5 min.

Figure 9 shows the results of the DOX release for both 22 nm **(Figure 9 (a))** and 50 nm **(Figure 9 (b))** core-sized NPs@DOX as a function of temperature (37-50°C) in DMEM. Each analysis was performed three independent times to ensure reproducibility.

Both systems exhibit a temperature-dependent increase in DOX release. Below 39 °C, only negligible release is observed, whereas a significant increase occurs above 40 °C, consistent with the LCST of the polymer in physiological medium. Although differences in release profiles are observed between 22 nm and 50 nm nanoparticles, these variations are most likely related to differences in polymer content and drug loading, rather than intrinsic differences in release kinetics. These results indicate that drug release is primarily governed by temperature-induced polymer transition rather than direct magnetic triggering.

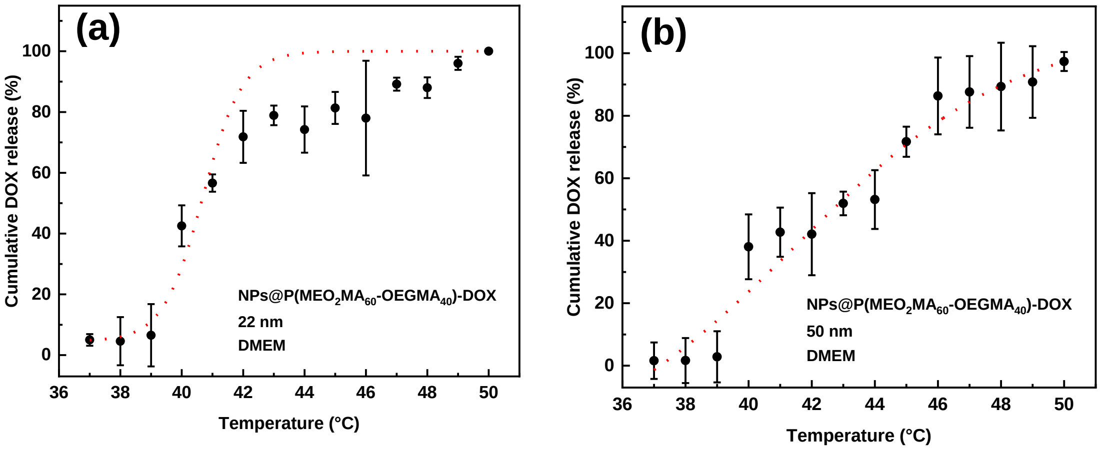

Figure 9 NPs@DOX release curves as a function of temperature in DMEM. (a) 22nm and (b) 50nm.

DOX release as function of time at 37 and 42°C:

In a previous study, we mentioned that beyond the LCST, the chains of the copolymer change their colloidal behavior from a swollen to a contracted state on the surface of the NPs. This transition is governed by the stability of the hydrogen interaction, which is broken by the mechanism at the level of hydrogen bonds with H_2O molecules. According to the obtained results, the grafted copolymer presented an LCST of 40°C in physiological medium (DMEM). At this temperature, the NPs @ DOX changed their behavior and began to release DOX. To determine the time required for the release of the total mass of the loaded DOX, we planned to study the release of DOX as a function of time from 1 to 50 h at two fixed temperatures: 37°C, which is the physiological temperature, and 42°C, which is the polymer LCST in DMEM. The results of this study are shown in **Figure 10**. Both 22 **(Figure 10 (a))** and 50 nm **(Figure 10 (b))** NPs @ DOX curves showed an increase in DOX release as a function of time.

At 37°C, the amount of DOX released in DMEM after one hour was 5% (a, b). During the fisrts 8 h, DOX was release slightly faster from 22 nm core-sized NPs (fig. 10a) than from 50 nm core-sized NPs (fig. 10b), reaching a cumulative release of 19 and 25 % respectively. Following the same trend, at this temperature, 50% of DOX release was achieved after 24 h for 22 nm core-sized NPs and 29 h for 50 nm core-sized NPs. After 50h at 37ºC, 60% and 70% of DOX was released from 22 and 50 nm core-sized NPs respectively. This release at physiological temperature indicates that partial drug diffusion occurs even below the LCST, likely due to incomplete confinement of DOX within the polymer network.

At 42°C, both 22 and 50 nm NPs @ DOX reported an immediate burst release, thus, after 1h we found 50% and 40% cumulative DOX release respectively. 50% cumulative DOX release was attained between 3 and 4 h in the case of 50 nm core-sized NPs, following the same slower release trend than at 37ºC. However, the DOX released from 50 nm NPs is slightly accelerated compared to 20 nm NPs release after 24 h of incubation. In any case, 100% DOX release is achieved after 50 h of incubation at 42ºC. This accelerated release at elevated temperature is attributed to the collapse of the polymer shell above the LCST, which enhances DOX diffusion from the polymer network. Although differences between the two NPs sizes (22 and 50nm) are observed, particularly in the early and late stages of release, these variations are mainly attributed to differences in drug loading capacity and polymer content rather than a fundamental change in the release mechanism. Therefore, NPs size mainly affects drug loading capacity, while the release mechanism remains similar for both systems.

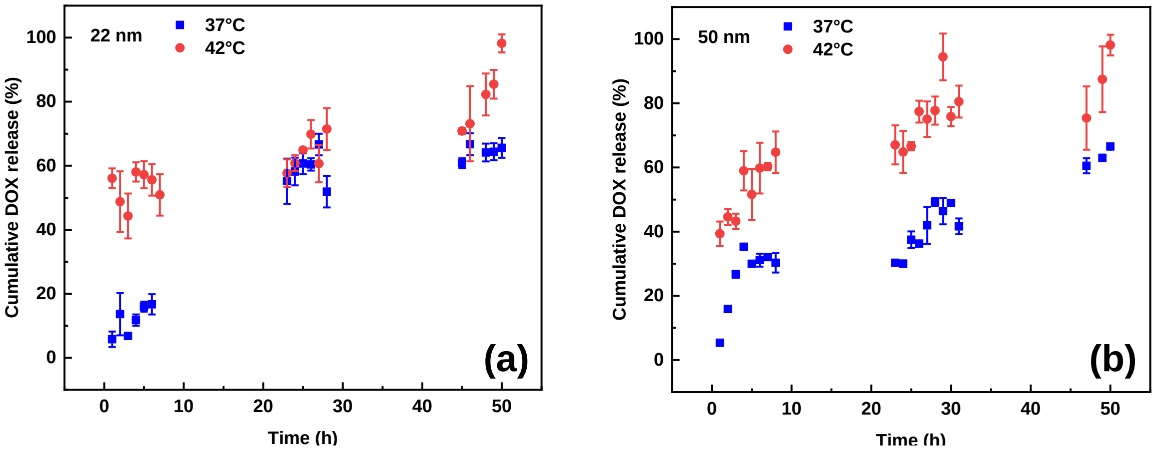

Figure 10: NPs@DOX release curves as a function of time in DMEM at 37ºC and 42ºC. 22nm (a) and 50nm (b).

To find out the release kinetic order of our NPs, the K_0, K_1 and K_h parameters of the zero-order, first-order, and Higuchi models, respectively, were calculated, as well as R^2 correlation coefficients. The corresponding kinetic parameters and correlation coefficients are presented in **Table 1**.

For both nanoparticle sizes, the zero-order kinetic model provides the best fit among the tested models, as indicated by the highest correlation coefficients. This suggests that DOX release rate is independent of the drug concentration encapsulated within the NPs, meaning that DOX is released in an approximately constant manner over time, despite its decreasing internal concentration (Ibrahim et al., 2022).

Table 1: DOX release kinetic data from 22 and 50nm NPs @P(MEO$_2$MA$_{60}$OEGMA$_{40}$) at 37°C and 42°C in DMEM.

NPs@ P(MEO2MA60OEGMA40) Size /température	**Zero order**		**First order**		**Higuchi**	
	K0	**R^2**	**K1**	**R^2**	**Kh**	**R^2**
22nm/37°C	**1,21033**	**0,92986**	**-0.02163**	**0.82966**	**2.70648**	**0.91864**
22nm/42°C	**0,67446**	**0,79273**	**-0.01949**	**0.7661**	**1.12731**	**0.71982**
50nm/37°C	**0,74956**	**0,92914**	**-0.0154**	**0.81511**	**2.91797**	**0.76788**
50nm/42°C	**0,8457**	**0,82184**	**-0.02649**	**0.8131**	**2.66878**	**0.81627**

The Drug Loading Capacity (DLC, wt%) and the Drug Loading Efficiency (DLE, wt%) values of 22 and 50 nm NPs@ P(MEO$_2$MA$_{60}$OEGMA$_{40}$) are shown in **Table 2**.

The 50 nm core-sized NPs@ P(MEO$_2$MA$_{60}$OEGMA$_{40}$) showed a higher DLC and DLE than 22 nm core-sized NPs@ P(MEO$_2$MA$_{60}$OEGMA$_{40}$). This is related to the higher polymer density in the 50 nm NPs shell, which was previously confirmed by TGA (fig. 3), since DOX is encapsulated in the polymeric shell. These results indicate that nanoparticle size primarily influences drug loading capacity rather than the intrinsic release kinetics.

Table 2: Drug Loading Capacity (DLC) and the Drug Loading Efficiency (DLE) of DOX-loaded NPs@ P(MEO$_2$MA$_{60}$OEGMA$_{40}$). Data were obtained from freshly prepared NPs.

Nanosystems	**Nanoparticles Diameters**	**DLC (wt%)**	**DLE (wt%)**
NPs @ P(MEO2MA60OEGMA40)	22	5,2	52,9
NPs @ P(MEO2MA60OEGMA40)	50	7	70,28

c- Magnetic hyperthermia studies:

The ability of NPs@ P($MEO_2MA_{60}OEGMA_{40}$) to heat up under an external magnetic field was also studied. **Figure 11** shows the heating curves of both 22 **(Figure 11-(a))** and 50 nm **(Figure 11-(b))** NPs@ P($MEO_2MA_{60}OEGMA_{40}$) as a function of time under an alternating magnetic field of 536.5 kHz / 300 Gauss (blue) and 796 kHz / 200 Gauss (red) in water (dashed lines) and DMEM (solid lines). Magnetic measurements showed that 22 and 50-nm NPs @ P($MEO_2MA_{60}OEGMA_{40}$) possess superparamagnetic properties. This explains their heating by both the Brown and Neel relaxation phenomena(Hallali, n.d.). These measurements also confirmed the influence of the NP size on their magnetic properties. The NPs with the largest size (50 nm) have greater magnetic properties than those with the smallest size (22 nm), which explains their heating properties when subjected to an external magnetic field. 22 nm NPs @ P($MEO_2MA_{60}OEGMA_{40}$) (a) present magnetic hyperthermia properties three times weaker than those of 50 nm diameter (b). 50 nm NPs @ P($MEO_2MA_{60}OEGMA_{40}$) show an increase of temperature of 3 and 2°C after only 160 s in water and DMEM respectively at 536.5 KHz (equivalent to an SAR of 57.81 and 53.21 W.g-1 respectively). This decrease in temperature can be explained by the presence of the P($MEO_2MA_{60}OEGMA_{40}$) copolymer on the surface of the NPs. These results show promising values compared with the results(Ferjaoui, n.d.) obtained previously by the team, which gave temperatures of 2 and 1.6°C in water and physiological medium after the same measurement time(Ferjaoui, n.d.). Concerning the influence of the medium, the NPs @ P($MEO_2MA_{60}OEGMA_{40}$) showed a lower heating temperature once they were dispersed in the culture medium than water. We have previously proved that the colloidal behavior of core/shell MNPs is driven by the copolymer chains grafted at their surfaces; once they are dispersed in a physiological medium (DMEM), the salts within the DMEM disrupt the hydration structure that surrounds the polymer chains, which decreases the hydrophilicity of the NPs and makes them less efficient in heating properties. In a previous section (**Figure 5**), we studied the effect of temperature on the colloidal behavior of both 22 and 50 nm NPs @ P($MEO_2MA_{60}OEGMA_{40}$), and we have reported the LCST behavior between 40 and 42°C. Heating the NPs to this temperature allows the release of the anti-cancer drug encapsulated on the NPs into the tumor.

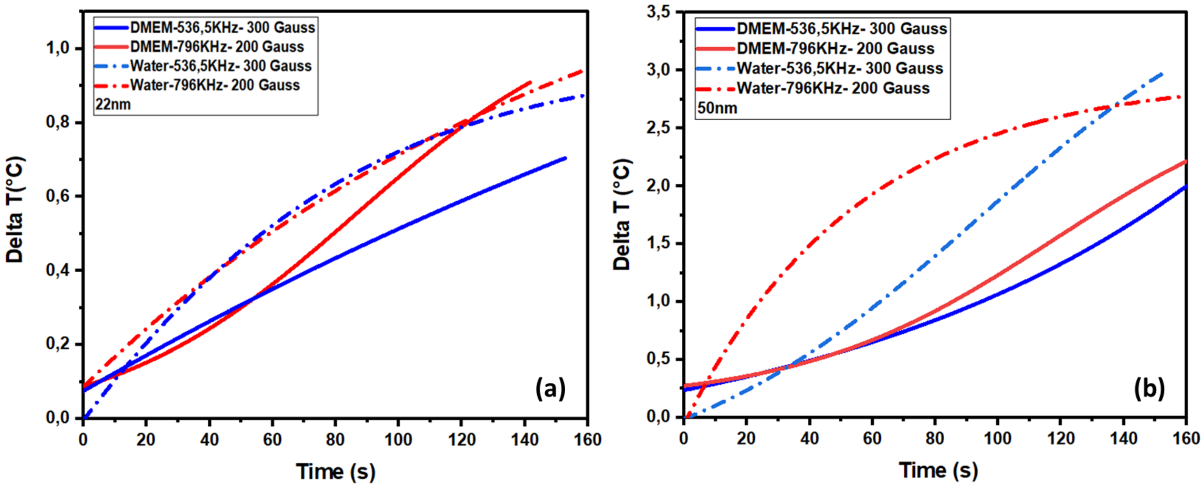

Figure 11: Temperatures of 22nm (a) and 50nm (b) NPs @ P(MEO$_2$MA$_{60}$OEGMA$_{40}$) under an alternating magnetic field in DMEM (solid line) and water (dashed lines) at 536.5 (blue) and 796 (red) KHz.

d- Cytotoxic effect of DOX@NPs:

To evaluate the potential of DOX-loaded NPs @ P(MEO$_2$MA$_{60}$OEGMA$_{40}$) as drug delivery systems their cytotoxicity was assessed against DOX-sensitive SKOV-3 ovarian cell line. To investigate the effect of ~~the~~ temperature-triggered DOX release, ~~to~~ two incubation conditions were considered: 37ºC as physiological control temperature, and 42ºC as a temperature above the LCST, where DOX release is ~~induced~~ activated, as discussed in the previous section **(Figure 9).** The results of these investigations on both 22 and 50nm sized NPs @ P(MEO$_2$MA$_{60}$OEGMA$_{40}$) are shown in **Figure 12.**

Based on the DOX release kinetics at 37ºC and 42ºC, incubation times were selected to ensure comparable cumulative DOX release under both conditions, namely 24 h at 37 °C and 5 h at 42 °C. Under these conditions, the cumulative DOX release was similar (approximately 60% for 22 nm DOX@NPs and 50% for 50 nm DOX@NPs), suggesting that the concentration of free DOX in the incubation medium is comparable for both temperatures **(Figure 10).**

The tested DOX concentrations ranged up to 5,29 and 7,46 µg for 22 **(Figure 12-(a))** and 50 nm **(Figure 12-(b))** DOX-loaded NPs @ P(MEO$_2$MA$_{60}$OEGMA$_{40}$) respectively, and equivalent concentration of free DOX were used as controls.

As shown in Figure 14, cell viability decreases progressively with increasing DOX concentration. Notably, DOX@NPs exhibit higher cytotoxicity compared to free DOX, and this effect is more pronounced for 50nm DOX@NPs than for 22nm DOW@NPs under both incubation conditions.

The enhanced cytotoxicity of DOX when delivered via NPs may be attributed to improved cellular uptake through NPs-mediated internalization pathways, as well as increased intracellular retention compared to free DOX.

In addition, the higher cytotoxicity observed for 50 nm DOX@NPs compared to 22 nm DOX@NPs is consistent with their higher drug loading capacity. Indeed, under the selected incubation conditions, the cumulative DOX release was approximately 60% for 22 nm DOX@NPs and 50% for 50 nm DOX@NPs, indicating that a larger fraction of DOX remains associated with the 50 nm NPs, which may contribute to enhanced intracellular delivery and cytotoxic effect.

To ensure that the observed cytotoxicity is primarily associated with DOX and not by the nanocarrier itself, the cytotoxicity of DOX-free 22 and 50 nm NPs @ $P(MEO_2MA_{60}OEGMA_{40})$ was also assessed. Equivalent concentrations of DOX-free NPs @ $P(MEO_2MA_{60}OEGMA_{40})$ were tested in SKOV-3 cells at 24 h (37ºC), 72h (37ºC) and 5 h (42ºC).

The results show that DOX-free NPs@ $P(MEO_2MA_{60}OEGMA_{40})$ induce only a slight decrease in cell viability for both 22 and 50 nm systems. The results show that DOX-free nanoparticles induce only a slight decrease in cell viability for both 22 nm and 50 nm systems. Cell viability remained above 80% for all tested concentrations and incubation conditions, except at the highest concentration (100 $\mu g \cdot mL^{-1}$), where viability values of approximately 77–78% were observed.

This slight decrease in cell viability can be explained by the increase of the concentration of the released metal ions from NPs, which can be cytotoxic to SKOV-3 cells (Mahmoudi et al., 2011) This cytotoxicity is due to the low solubility of Fe^{2+}/Fe^{3+} ions at physiological pH when their concentration increases above a critical threshold(Quignard, n.d.), which causes mitochondrial disruption that can give rise to various tissue reactions, such as the generation of reactive oxygen species (ROS), which can lead to cell death(Saeki et al., 1976). It should be noted that control experiments at 42 °C in the absence of nanoparticles would be required to fully decouple the effect of temperature alone from nanoparticle-mediated drug delivery.

However, the reduction in cell viability observed for DOX@NPs is significantly higher than that induced by DOX-free NPs@$P(MEO_2MA_{60}OEGMA_{40})$, suggesting that the cytotoxic effect is primarily driven by DOX delivery and supporting the potential of this thermoresponsive nanocarrier for controlled drug delivery in cancer therapy.

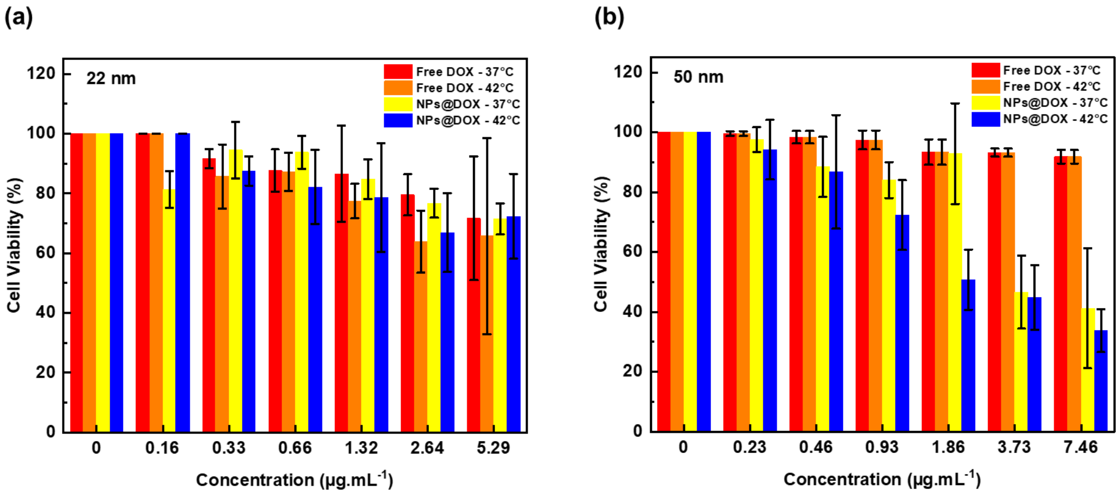

Figure 12 : Viability of SKOV-3 cells after 24 h at 37 °C (yellow) and 5 h at 42 °C (blue) following exposure to DOX-loaded 22 nm NPs@P($MEO_2MA_{60}OEGMA_{40}$) (a) and 50 nm NPs@P($MEO_2MA_{60}OEGMA_{40}$) (b), as well as free DOX (red and orange).

3- Conclusion:

Two different sizes of iron oxide magnetic thermoresponsive core/shell NPs @ P($MEO_2MA_{60}OEGMA_{40}$) were successfully synthesized via ARGET ATRP without any effect on the crystalline structure of the magnetic core ($Zn_{0.4}Fe_{2.6}O_4$@ $MnFe_2O_4$) NPs.

The temperature-responsive behavior of the copolymer by DLS analysis. demonstrating a transition from a hydrophilic to a hydrophobic state. This thermally induced phase transition enables efficient encapsulation of doxorubicin (DOX) and its controlled release upon heating.

DOX release studies further confirmed the temperature-dependent release behavior and allowed evaluation of drug loading and release efficiency. In addition, the magnetic nanoparticles exhibited superparamagnetic behavior and efficient heating under an external alternating magnetic field, confirming their suitability for magnetic hyperthermia applications

Cytotoxicity assays demonstrated that both 22 and 50 nm NPs@P($MEO_2MA_{60}OEGMA_{40}$) are not cytotoxic towards ovarian cancer cells (SKOV-3) at concentrations of up to 50µg.mL^{-1}with DOX-loaded nanoparticles showing higher anticancer activity compared to free DOX, highlighting the benefit of nanoparticle-mediated drug delivery.

Overall, these results demonstrate the potential of these thermoresponsive magnetic nanocarriers as multifunctional platforms for combined drug delivery and magnetic hyperthermia applications. Further studies, including in vivo evaluation and mechanistic investigations of cellular uptake, would be required to fully assess their translational potential.

5- References:

Abenojar, E.C., Wickramasinghe, S., Bas-Concepcion, J., Samia, A.C.S., 2016. Structural effects on the magnetic hyperthermia properties of iron oxide nanoparticles. Prog. Nat. Sci. Mater. Int. 26, 440–448. https://doi.org/10.1016/j.pnsc.2016.09.004

Angelopoulou, A., Kolokithas-Ntoukas, A., Fytas, C., Avgoustakis, K., 2019. Folic Acid-Functionalized, Condensed Magnetic Nanoparticles for Targeted Delivery of Doxorubicin to Tumor Cancer Cells Overexpressing the Folate Receptor. ACS Omega 4, 22214–22227. https://doi.org/10.1021/acsomega.9b03594

Cotin, G., Blanco-Andujar, C., Nguyen, D.-V., Affolter, C., Boutry, S., Boos, A., Ronot, P., Uring-Lambert, B., Choquet, P., Zorn, P.E., Mertz, D., Laurent, S., Muller, R.N., Meyer, F., Felder Flesch, D., Begin-Colin, S., 2019. Dendron based antifouling, MRI and magnetic hyperthermia properties of different shaped iron oxide nanoparticles. Nanotechnology 30, 374002. https://doi.org/10.1088/1361-6528/ab2998

Dine, E.J.A., n.d. Synthèse et caractérisation des nanoparticules intelligentes 226.

Doberenz, F., Zeng, K., Willems, C., Zhang, K., Groth, T., 2020. Thermoresponsive polymers and their biomedical application in tissue engineering – a review. J. Mater. Chem. B 8, 607–628. https://doi.org/10.1039/C9TB02052G

Ferjaoui, Z., n.d. Synthèse et caractérisation de nanoparticules magnétiques répondantes pour des applications en thérapie cancéreuse.

Ferjaoui, Z., Jamal Al Dine, E., Kulmukhamedova, A., Bezdetnaya, L., Soon Chang, C., Schneider, R., Mutelet, F., Mertz, D., Begin-Colin, S., Quilès, F., Gaffet, E., Alem, H., 2019. Doxorubicin-Loaded Thermoresponsive Superparamagnetic Nanocarriers for Controlled Drug Delivery and Magnetic Hyperthermia Applications. ACS Appl. Mater. Interfaces 11, 30610–30620. https://doi.org/10.1021/acsami.9b10444

Ferjaoui, Z., Schneider, R., Meftah, A., Gaffet, E., Alem, H., 2017a. Functional responsive superparamagnetic core/shell nanoparticles and their drug release properties. RSC Adv. 7, 26243–26249. https://doi.org/10.1039/C7RA02437A

Ferjaoui, Z., Schneider, R., Meftah, A., Gaffet, E., Alem, H., 2017b. Functional responsive superparamagnetic core/shell nanoparticles and their drug release properties. RSC Adv. 7, 26243–26249. https://doi.org/10.1039/C7RA02437A

Hallali, N., n.d. Utilisation de nanoparticules magnétiques dans les traitements anti-tumoraux: Au-delà de l'hyperthermie magnétique 207.

Ibrahim, M., Abuwatfa, W.H., Awad, N.S., Sabouni, R., Husseini, G.A., 2022. Encapsulation, Release, and Cytotoxicity of Doxorubicin Loaded in Liposomes, Micelles, and Metal-Organic Frameworks: A Review. Pharmaceutics 14, 254. https://doi.org/10.3390/pharmaceutics14020254

Jamal Al Dine, E., Ferjaoui, Z., Ghanbaja, J., Roques-Carmes, T., Meftah, A., Hamieh, T., Toufaily, J., Schneider, R., Marchal, S., Gaffet, E., Alem, H., 2017. Thermoresponsive magnetic Fe 3 O 4 @P(MEO 2 MA X -OEGMA 100-X) NPs and their applications as drug delivery systems. Int. J. Pharm. 532, 738–747. https://doi.org/10.1016/j.ijpharm.2017.09.019

Jurgons, R., Seliger, C., Hilpert, A., Trahms, L., Odenbach, S., Alexiou, C., 2006. Drug loaded magnetic nanoparticles for cancer therapy. J. Phys. Condens. Matter 18, S2893–S2902. https://doi.org/10.1088/0953-8984/18/38/S24

Kievit, F.M., Zhang, M., 2011. Surface Engineering of Iron Oxide Nanoparticles for Targeted Cancer Therapy. Acc. Chem. Res. 44, 853–862. https://doi.org/10.1021/ar2000277

Li, L., Jiang, W., Luo, K., Song, H., Lan, F., Wu, Y., Gu, Z., 2013. Superparamagnetic Iron Oxide Nanoparticles as MRI contrast agents for Non-invasive Stem Cell Labeling and Tracking. Theranostics 3, 595–615. https://doi.org/10.7150/thno.5366

Louaguef, D., Medjahdi, G., Diliberto, S., Seemann, K.M., Gries, T., Bizeau, J., Mertz, D., Gaffet, E., Alem, H., 2025. Improving magnetic properties of Mn- and Zn-doped core–shell iron oxide nanoparticles by tuning their size. Beilstein J. Nanotechnol. 16, 2285–2295. https://doi.org/10.3762/bjnano.16.157

Mahmoudi, M., Hofmann, H., Rothen-Rutishauser, B., Petri-Fink, A., 2012. Assessing the In Vitro and In Vivo Toxicity of Superparamagnetic Iron Oxide Nanoparticles. Chem. Rev. 112, 2323–2338. https://doi.org/10.1021/cr2002596

Mahmoudi, M., Sant, S., Wang, B., Laurent, S., Sen, T., 2011. Superparamagnetic iron oxide nanoparticles (SPIONs): Development, surface modification and applications in chemotherapy. Adv. Drug Deliv. Rev. 63, 24–46. https://doi.org/10.1016/j.addr.2010.05.006

Nguyen, K.T., 2011. Targeted Nanoparticles for Cancer Therapy: Promises and Challenges. J. Nanomedicine Nanotechnol. 02. https://doi.org/10.4172/2157-7439.1000103e

Pasparakis, G., Tsitsilianis, C., 2020. LCST polymers: Thermoresponsive nanostructured assemblies towards bioapplications. Polymer 211, 123146. https://doi.org/10.1016/j.polymer.2020.123146

Périgo, E.A., Sampaio, F.A., De Campos, M.F., 2013. On the specific absorption rate of hyperthermia fluids. Appl. Phys. Lett. 103, 264107. https://doi.org/10.1063/1.4860966

Quignard, S., n.d. Comportement des nanoparticules de silice en milieu biologique: des cellules aux biomatériaux.

Sadhukha, T., Wiedmann, T.S., Panyam, J., 2013. Inhalable magnetic nanoparticles for targeted hyperthermia in lung cancer therapy. Biomaterials 34, 5163–5171. https://doi.org/10.1016/j.biomaterials.2013.03.061

Saeki, S., Kuwahara, N., Nakata, M., Kaneko, M., 1976. Upper and lower critical solution temperatures in poly (ethylene glycol) solutions. Polymer 17, 685–689. https://doi.org/10.1016/0032-3861(76)90208-1

Saha, V., Cheah, P., Saha, R., Zhao, Y., Biswas, G., 2025. APTES modified magnetite nanoparticles as a theranostic nanocarrier: a study of loading and sustained release of daunorubicin. Mater. Adv. 6, 6843–6855. https://doi.org/10.1039/D5MA00514K

Santhosh, P.B., Ulrih, N.P., 2013. Multifunctional superparamagnetic iron oxide nanoparticles: Promising tools in cancer theranostics. Cancer Lett. 336, 8–17. https://doi.org/10.1016/j.canlet.2013.04.032

Santos, A.C., Alves, S.P.C., Carvalhão, G., Correia, N.T., Viciosa, M.T., Farinha, J.P.S., 2021. Phase diagrams of temperature-responsive copolymers p(MEO2MA-co-OEGMA) in water. Polymer 228, 123858. https://doi.org/10.1016/j.polymer.2021.123858

Shi, Y., Zhang, Y., Zhu, L., Miao, Y., Zhu, Y., Yue, B., 2024. Tailored Drug Delivery Platforms: Stimulus-Responsive Core–Shell Structured Nanocarriers. Adv. Healthc. Mater. 13, 2301726. https://doi.org/10.1002/adhm.202301726

Wang, C., Shaw, L.L., 2014. On synthesis of Fe2SiO4/SiO2 and Fe2O3/SiO2 composites through sol–gel and solid-state reactions. J. Sol-Gel Sci. Technol. 72, 602–614. https://doi.org/10.1007/s10971-014-3483-5

Yigit, M.V., Moore, A., Medarova, Z., 2012. Magnetic Nanoparticles for Cancer Diagnosis and Therapy. Pharm. Res. 29, 1180–1188. https://doi.org/10.1007/s11095-012-0679-7

Zhang, H., Liu, X.L., Zhang, Y.F., Gao, F., Li, G.L., He, Y., Peng, M.L., Fan, H.M., 2018. Magnetic nanoparticles based cancer therapy: current status and applications. Sci. China Life Sci. 61, 400–414. https://doi.org/10.1007/s11427-017-9271-1